# Phase diagram and structure evolution mechanism in ultrahigh energy storage $NaNbO_3$-based superparaelectric relaxor ferroelectric ceramics

Kai Dai (戴凯),[1] Yafang Li (李亚芳),[1] Yuting Yan (严雨婷),[1] Zhen Liu (刘振),[2] Anyang Cui (崔安阳),[3] Kai Jiang (姜凯),[1] Liyan Shang (商丽燕),[1] Yawei Li (李亚巍),[1] Genshui Wang (王根水),[2] and Zhigao Hu (胡志高)[1,4,*]

[1]*Technical Center for Multifunctional Magneto-Optical Spectroscopy (Shanghai), Engineering Research Center of Nanophotonics & Advanced Instrument (Ministry of Education), Department of Physics, School of Physics and Electronic Science, East China Normal University, Shanghai 200241, China*

[2]*Key Laboratory of Inorganic Functional Materials and Devices, Shanghai Institute of Ceramics, Chinese Academy of Sciences, Shanghai 200050, China*

[3]*Key Laboratory of Optoelectronic Material and Device, Department of Physics, Shanghai Normal University, Shanghai 200234, China*

[4]*Collaborative Innovation Center of Extreme Optics, Shanxi University, Taiyuan, Shanxi 030006, China*

(Received 11 December 2023; revised 21 April 2024; accepted 29 April 2024; published 13 May 2024)

The construction of superparaelectric (SPE) systems has been demonstrated to be an essential means of enhancing energy storage properties, while the underlying physical behavior is still unclear. Here, the structure evolution of SPE was investigated on $(1\text{-}x)(0.85NaNbO_3\text{-}0.15Sr_{0.7}Bi_{0.2}TiO_3)\text{-}xBi(Mg_{0.5}Zr_{0.5})O_3$ (NN-SBT-BMZ) ceramics by analyzing the lattice structure and electronic transitions behavior under the regulation of chemical content and temperature. The cell volume and optical band gap has been enhanced significantly, with increasing the doping contents. Moreover, the detailed phase diagram of NN-SBT-BMZ with a temperature content was derived by combining the evolution of dielectric, optical transitions, lattice structure, and phonon behavior under thermodynamic field, in which the evolution of the lattice structure is closely related to the domain structure. Noteworthy, the oscillatory processes of the main phonons near the $T_B$ temperature clearly reflect the relaxation state of the lattice structure, which is caused by the fact that the static displacements of the atoms in the crystal with respect to their equilibrium positions do not occur simultaneously. This work describes the comprehensive study of structural properties on $NaNbO_3$-based SPE ceramics, which display positive implications for the development of energy storage capacitors.

DOI: 10.1103/PhysRevB.109.195204

## I. INTRODUCTION

Dielectric energy storage has great prospects for development in electronic devices and power systems due to the advantages of rapid charging and discharging speed and ultrahigh energy storage density [1–5]. A number of studies have been conducted on dielectric materials, such as linear dielectric, paraelectric (PE), ferroelectric, and antiferroelectric in the applications of energy storage capacitors, where the most effective way to enhance the energy storage density and efficiency of dielectrics is to induce ferroelectric to the relaxor ferroelectrics (RFEs) [6–10]. The long-range ordered micrometer ferroelectric domains are turned into short-range ordered nanodomains by ion doping and solid solution in ferroelectrics, which weakens the domain mutual coupling, lowers the domain switching energy barriers, and increases the local heterogeneity [11–15]. However, there is still visible hysteresis in the nanodomain switching procedure, which has been a bottleneck to further improving the energy storage performance. Recently, a novel strategy known as superparaelectric (SPE) engineering has been demonstrated to be extremely successful in enhancing the energy storage performance [4,16–19]. The nanodomains are further reduced and the interdomain coupling is further weakened in the SPE state, which makes the domain switching energy barrier equivalent to the thermal perturbation energy, allowing for minimal hysteresis.

$NaNbO_3$ with a complex crystal structure and undergoing varieties of phase transformations under external field is considered as a promising material for lead-free energy storage dielectric. Although it is generally recognized that there are seven main phases of $NaNbO_3$ under the action of temperature fields: $U \rightarrow T_2 \rightarrow T_1 \rightarrow S \rightarrow R \rightarrow P \rightarrow N$, while the complicated temperature-driven structure also indicates a huge possibility of performance modulation [20–23]. $NaNbO_3$ exhibits irreversible electric field-induced antiferroelectric-ferroelectric structure transition and large residual polarization at room temperature, which obtains a poor energy storage performance. Fortunately, the performance of $NaNbO_3$-based ceramics can be effectively improved by adjusting the chemical modification, while the $NaNbO_3$-$(Sr, Bi)TiO_3$-$Bi(Mg, Zr)O_3$ SPE ceramics have been proven to realize an ultrahigh energy storage density of 7.59 J $cm^{-3}$ and a high efficiency of 81.3% simultaneously [24]. Simultaneously, the majority of ferroelectrics exhibit a unique behavior of external field-induced structural transformations accompanied by huge energy storage and

*zghu@ee.ecnu.edu.cn

 

release, while the transformation of the structure of dielectric ceramics is closely related to the study of energy storage mechanisms. However, the evolution of the lattice structure for SPE ceramics is still unclear, which significantly limits the development of energy storage ceramics. The condensed matter spectroscopy methods have been shown to yield numerous important physical evidences for the structural properties of typical ferroelectrics or antiferroelectrics, such as lattice dynamics and optical transition, etc. [25–29], while the investigation of the SPE structure is still lacking. Therefore, there is an urgent need to probe the *in situ* structural evolution of SPE ceramics, which is also crucial to explore their structural and functional stability, as well as to determine the underlying structural transition mechanisms.

In this work, the lattice symmetry, phonon behavior, and optical transition of SPE $(1\text{-}x)(0.85NaNbO_3\text{-}0.15Sr_{0.7}Bi_{0.2}TiO_3)\text{-}xBi(Mg_{0.5}Zr_{0.5})O_3$ (NN-SBT-BMZ) under doping and temperature have been systematically investigated. The cell volume and the optical band gap are significantly enhanced as increasing the doping component. The evolution of the lattice parameters and the band gap under the temperature field may be related to the variation of the NN-SBT-BMZ domain structure, while the interdomain coupling is significantly weakened as the temperature increases. Moreover, the oscillatory processes of the main phonons near the $T_B$ temperature was discovered by the Raman spectra. Eventually, a clear structural evolution has been exactly drawn due to the thermally induced dielectric, lattice parameter, phonon behavior, and optical band gap ($E_g$) evolution process, while the RFE/SPE phase boundary at room temperature is useful for enhancing the energy storage density. This work can deepen the comprehension of the structure evolution for SPE ones by condensed matter spectroscopy, which will facilitate the development of SPE energy storage ceramics.

## II. MATERIALS AND METHODS

The NN-SBT-BMZ ceramics are obtained via a solid-state reaction approaches, while the detailed procedure of the preparation can be found in the literature [24]. Samples of $x = 0.04$, 0.08, 0.12, and 0.16 are denoted as NN-SBT-BMZ04, NN-SBT-BMZ08, NN-SBT-BMZ12, and NN-SBT-BMZ16, respectively.

The structure of NN-SBT-BMZ ceramics was explored by x-ray diffraction (XRD) (Japan SmartLab), with a Cu K$\alpha$ rotating source. The molecular vibrational behavior was studied by the micro-Raman spectrometer (Jobin-Yvon LabRAM HR Evolution, Horiba) using an ultralow frequency attachment over the frequency ranges of 5–1000 $cm^{-1}$, while a laser with the wavelength of 532 nm was selected as the excitation source. Temperature-dependent Raman scattering experiment (80–800 K) was performed by the Linkam THMSE 600 heating/cooling stage. The temperature effect has been calibrated by the Bose-Einstein equation [30]: $n(\omega, T) = [\exp(\hbar\omega/kT) - 1]^{-1}$, in which the $\hbar$, $\omega$, $k$, and $T$ stand for Planck constant, phonon wave number, Boltzmann constant, and the temperature, respectively. The optical transition property was investigated on a visible UV spectroscopic ellipsometer (V-VASE by J. A. Woolam Co., Inc.) in the photon energy range of 1.24–4.96 eV, in which the incident angle was kept at 70°. Temperature-dependent spectroscopic ellipsometry (SE) (300–600 K) was accomplished by the Instec cell with a cooling accessory, while the experimental error induced by the window during the test has been eliminated.

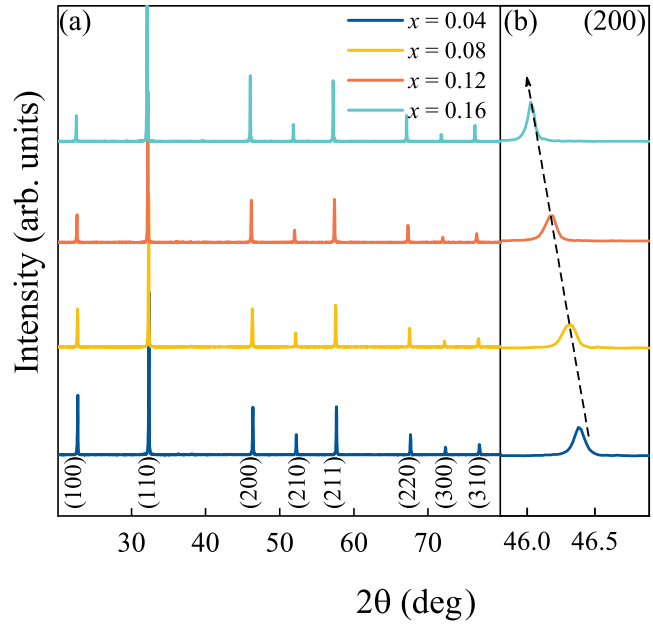


FIG. 1. (a) The XRD patterns of NN-SBT-BMZ ceramics and (b) an enlarged region near (200) diffraction peak.

## III. RESULTS AND DISCUSSION

Figure 1(a) depicts the XRD pattern of the NN-SBT-BMZ ceramics, in which all samples were pure perovskite structures exhibiting a single peak at room temperature, with no obvious secondary phases. The diffraction peaks gradually move to a lower angle with increasing the $Bi(Mg_{0.5}Zr_{0.5})O_3$ (BMZ) content, while the evolution of (200) diffraction peaks shown in Fig. 1(b), marking the gradual expansion of the lattice structure. This is a result of the occupation of the A site by the larger $Bi^{3+}$ and the B site by the larger $Mg^{2+}$ and $Zr^{4+}$ [31–33]. In order to further determine the evolution law of the cell parameters with the doping components, a refinement of the lattice structure was carried out with the $Pm\bar{3}m$ model. The fitting results are shown in Fig. 2(a), where the fitted data are well matched with the experimental spectra. The lattice parameter gradually increases from 3.919 Å to 3.945 Å with the elevation of the doping component, as shown in Fig. 2(b).

To probe more structure details in NN-SBT-BMZ ceramics, the lattice evolution with increasing the BMZ content was summarized by Raman-active phonon kinetics. Raman-active modes at low frequencies (<200 $cm^{-1}$) shown in Fig. 3(a) belong to the vibrations of the A-site cations, while the high-frequency region (>200 $cm^{-1}$) is mainly associated with the vibration of the B-O and $BO_6$ octahedrons. The strong peaks near 230 $cm^{-1}$ and 600 $cm^{-1}$ are allocated to the $F_{2g}$ ($\nu_5$) and $A_{1g}$ ($\nu_1$) phonon modes, respectively, which represent the critical vibrational behaviors of the $BO_6$ octahedron [25–29]. It is worth noting the peak at 850 $cm^{-1}$ is the

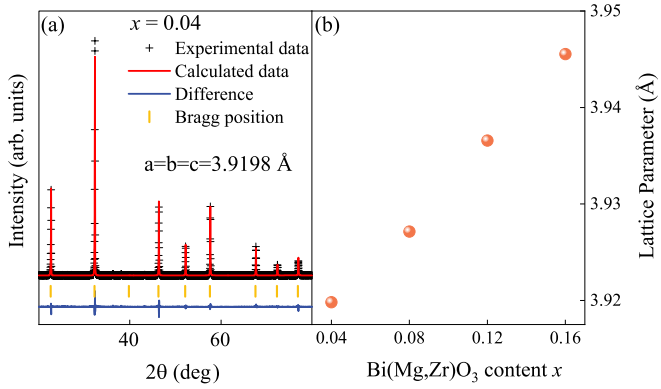


FIG. 2. (a) The refined spectra of NN-SBT-BMZ04 ceramics. (b) The content dependence of lattice parameters.

anharmonic coupling mode of $\nu_1$ and $\nu_5$, where the peak position appears significantly red shifted with increasing the BMZ content. To further investigate the evolution of lattice behavior, the BMZ content dependence of main phonon frequencies is shown in Fig. 3(b). It is apparent that the frequencies of the main phonon modes display decreasing phenomenon with increasing the BMZ content, which indicates that the hybridization between the Nb/Ti/Zr/Mg 3d and the O 2p orbitals is weakened. On one hand, it may be due to the variation of the cell parameters caused by the doping of BMZ. On the other hand, it could be attributed to the different bonding forces caused by the difference in the radii of the different ions. The doping of BMZ further breaks the equilibrium symmetry of the lattice structure, leading to the reduction for the frequency of phonon vibration modes. From this perspective, the BMZ introduction takes an important part in the lattice dynamic of $NaNbO_3$-based ceramics.

The investigation of the optical transition behavior is significant for understanding the intrinsic electronic structure of NN-SBT-BMZ ceramics, which can be revealed by SE. The multilayer superposition model (air/rough/ceramic) was developed to fit the sample spectra. The ceramic layer is modeled by the Tauc-Lorentz (TL) and Lorentz oscillator superposition, while the formula of the TL oscillator have

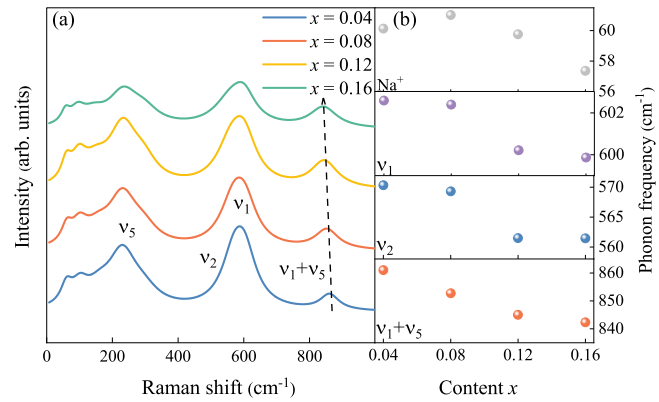


FIG. 3. (a) Raman spectra of the NN-SBT-BMZ ceramics at room temperature. (b) The frequency evolution of the main phonon with the doping of BMZ.

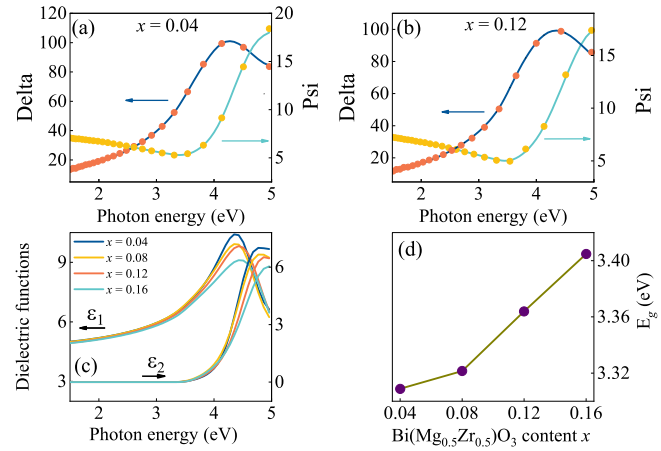


FIG. 4. The experimental ellipsometric (points) and best-fit (solid line) spectra for (a) NN-SBT-BMZ04 and (b) NN-SBT-BMZ12, respectively. (c) The dielectric functions ($\varepsilon_1$ and $\varepsilon_2$) of the NN-SBT-BMZ ceramics. (d) The evolution of optical bandgap with increasing the BMZ content.

provided by [34]: $\varepsilon_1(E) = \varepsilon_\infty + \frac{2}{\pi} \mathrm{P} \int_{E_g}^{\infty} \frac{\xi \pi \varepsilon_2(\xi)}{\xi^2 - E^2} d\xi$, $\varepsilon_2(E) = \frac{AE_nC(E-E_g)^2}{(E^2-E_n^2)^2+C^2E^2} \frac{1}{E} (E \geqslant E_g)$, $\varepsilon_2(E) = 0$ $(E < E_g)$. The P is expressed as the Cauchy principal part of the integral, $E$ is represented as the incident photon energy, and $\varepsilon_\infty$ is referred to the high-frequency dielectric constant. The parameters $E_g$, $A$, $E_n$, and $C$ are the optical band gap, amplitude, peak position energy, and broadening term, respectively. The fitting spectra matched well with the experimental spectra depicted in Figs. 4(a)–4(b), while the best-fit parameters of NN-SBT-BMZ ceramics are displayed in Table I. The dielectric functions ($\varepsilon_1$ and $\varepsilon_2$) of the NN-SBT-BMZ ceramics were shown in Fig. 4(c). The imaginary part of dielectric functions ($\varepsilon_2$) is nearly zero below the absorption edge, suggesting that no additional electron transitions are detected in the low-energy range. The sudden increase of $\varepsilon_2$ with the increasing energy denotes the strong absorption, caused by the interband electron transitions between the valence band maximum to the conduction band minimum. Moreover, the $E_g$ parameter were extracted in the TL oscillator to quantify the evolution of the band gap. It is obvious that the band gap is enhanced with the increasing BMZ content shown in Fig. 4(d), which provides a positive effect on the increase of the breakdown field and energy storage density [24,28]. It is worth noting that the B-site cation arrangement and oxygen vacancies take an essential part in the energy band engineering of the perovskite structure [35]. Due to the A-site-deficient composition $Sr_{0.7}Bi_{0.2}TiO_3$ tends to introduce oxygen vacancies, while the formation of oxygen vacancies is inhibited by the presence of $Mg^{2+}$ ions. The enhancement of free carriers in NN-SBT-BMZ ceramic breaks the equilibrium of the lowest energy level in the conduction band energy level. The number of free carriers vacancies are reduced with the elevation of the BMZ doping fraction, which also requires an enhancement capability to induce electron transition behavior [36,37]. Simultaneously, the doping of BMZ changes the ordering of the B site and forms the Mg/Zr-O bond, which affects the optical transition behavior for the NN-SBT-BMZ samples.

TABLE I. The optimal SE fitting parameters of Lorentz and Tauc-Lorentz oscillators in NN-SBT-BMZ ceramics at room temperature. The fitting errors have been provided by (±).

| Sample | $E_g$ (eV) | $B_{r1}$ | $E_{n1}$ (eV) | $A_1$ | $C_2$ | $E_{n2}$ (eV) | $A_2$ |
|---|---|---|---|---|---|---|---|
| $x = 0.04$ | 3.30 | 0.58 | 4.64 | 3.45 | 1.97 | 5.39 | 108.4 |
| | ±0.03 | ±0.02 | ±0.01 | ±0.20 | ±0.09 | ±0.05 | ±8 |
| $x = 0.08$ | 3.32 | 0.61 | 4.67 | 2.85 | 3.06 | 5.39 | 139.5 |
| | ±0.03 | ±0.04 | ±0.01 | ±0.26 | ±0.18 | ±0.11 | ±13.7 |
| $x = 0.12$ | 3.36 | 0.72 | 4.83 | 3.78 | 5.62 | 5.92 | 171.4 |
| | ±0.04 | ±0.05 | ±0.02 | ±0.45 | ±0.7 | ±0.23 | ±14.6 |
| $x = 0.16$ | 3.40 | 0.78 | 4.88 | 3.17 | 10.98 | 5.88 | 288.4 |
| | ±0.02 | ±0.04 | ±0.02 | ±0.23 | ±1.11 | ±0.34 | ±60.1 |

RFEs are featured with a diffusive phase transformation over a wide temperature range, which covers from the Burns temperature where the nanodomains appear ($T_B$), to the intermediate temperature where the nanodomains grow and the maximum value of the dielectric constants ($T_m$), and finally to the freezing temperature where the nanodomains freeze ($T_f$) [38]. The relaxor ferroelectrics possess a common feature that the arrangement of different ions at crystallographic equivalence sites possesses disorder. The $Mg^{2+}$, $Zr^{2+}$, $Ti^{4+}$, and $Nb^{5+}$ ions are completely or partially disordered in the B site of the $ABO_3$ structure, which is expressed as $A(B'_{1/2}B''_{1/2})O_3$. Due to the difference in charge and size of B′ and B″, the structure has the lowest elastic and electrostatic energy, forming a completely symmetric structure. As the temperature drops below $T_B$, the system becomes an ergodic relaxation state. Despite the ferroelectric character, the overall features remain pseudocubic structure with structural transformations in certain regions. During the cooling process, the ferroelectric transition occurs first at higher Curie temperatures due to the disordered nature of the composition, which generates PNRs. The polarization orientation is randomly distributed due to the random motion of the PNRs, while the system quickly traverses the positions and returns to the state with the lowest free energy under any external action (temperature, electric field). The existence of PNRs and its evolutionary laws have been cleverly verified by refractive index (secondary electron effect) and Raman scattering spectra [39,40]. The studies on dielectric are mainly focused on the temperature range of $T_f$-$T_m$ for the conventional RFEs. There are fewer studies in the temperature range of $T_m$-$T_B$ for the SPE RFEs. The nanodomains are further reduced and the interdomain coupling is further decreased in the SPE state so that the domain switching energy barrier is equivalent to or lower than the thermal perturbation energy kT [41]. The polarization of nanodomains can be switched between energy-equivalent directions with high dynamics, resulting in enhanced energy storage density of the dielectric [42]. It is worth noting that the domain structure of PNRs is usually on the nm scale. However, the spectroscopic characterisation tools are all measured in μm scale. As the XRD results indicate, the lattice structure is pseudocubic phase and the diffraction peaks are all in a single peak. Therefore, the evolution of the average structure can be probed by condensed matter spectroscopy.

The determination of the dielectric constant-temperature curve is essential for understanding the structural evolution and determining the transition temperature. Figures 5(a)–5(b) depict the evolution pattern of the dielectric constant of NN-SBT-BMZ ceramics under thermal field at 1 kHz frequency. It is observed that the dielectric constants of NN-SBT-BMZ decreases significantly with the elevation of the BMZ doping fraction, while the dielectric peak gradually becomes broader, which should be attributed to the enhancement of the relaxation degree. In the $NaNbO_3$-based system, the doping cations will establish random localized electric and strain fields due to the mismatch of atomic size, mass, and electronegativity. There are fewer disturbed clusters when the substitutional cation concentration is lower than the critical threshold, yet every cluster can reach the maximum size, while the system maintains a long-range ordered ferroelectric behavior. However, the number of clusters increases but cannot achieve the maximum dimensions when the doping concentration nears and surpasses the threshold. The presence of tiny clusters leads to the dispersion and relaxation behavior for the system dielectric constant, where the short-range interactions between polar nanodomains are significantly enhanced. To

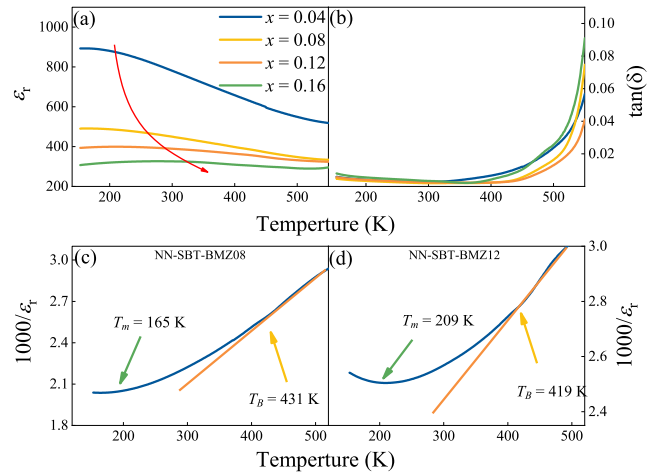


FIG. 5. Temperature-dependent (a)$\varepsilon_r$ and (b) tan $\delta$ for NN-SBT-BMZ ceramics at 1 KHz. The $T_B$ and $T_m$ temperatures of calculated from the Curie-Weiss law of (c) NN-SBT-BMZ08 and (d) NN-SBT-BMZ12.

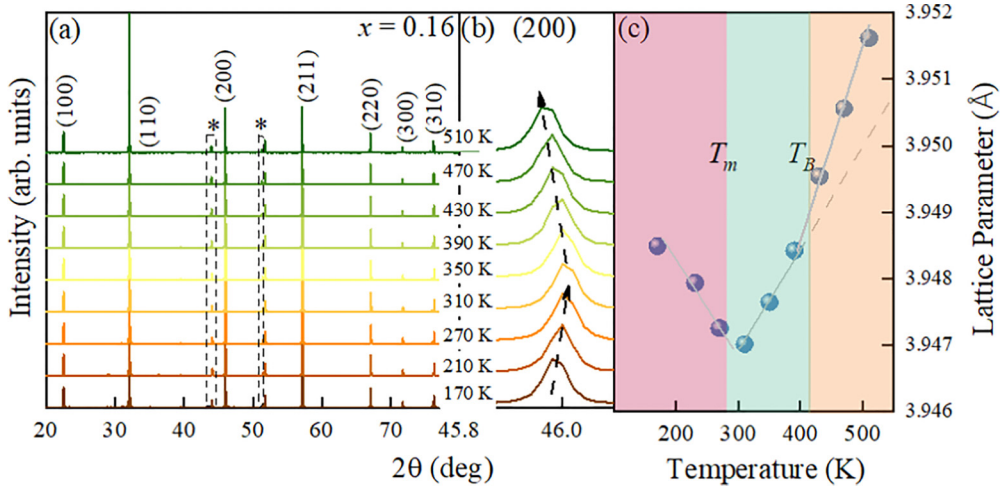


FIG. 6. (a) Temperature-dependent *in situ* XRD patterns of NN-SBT-BMZ16 ceramics, where the peaks of the sample table are assigned by (*). (b) The enlarged (200) plane from XRD patterns at different temperatures. (c) Temperature dependence of lattice parameters.

further determine the relaxation temperature ranges of different doping components, the corresponding $T_m$ as well as $T_B$ temperatures were obtained by Curie-Weiss law. The physical significance of $T_B$ is equivalent to the nucleation temperature of polar nanodomains, and the ferroelectric materials show relaxation properties only below $T_B$. $T_B$ exhibits a gradual decrease with increasing BMZ doping, while the $T_m$ evolves in the opposite direction. In addition, all ceramics show ergodic relaxation properties over a wide temperature range (from 200 K to $T_B$), which also indicates the good temperature stability of NN-SBT-BMZ ceramics.

Temperature-dependent XRD was employed to elucidate the thermal evolution of the lattice structure of NN-SBT-BMZ ceramics. It is worth noting that all diffraction peaks shown in Fig. 6(a) exhibit no annihilation with increasing the temperature. The enlarged (002) diffraction peaks and lattice parameters of NN-SBT-BMZ16 were displayed in Fig. 6(b) and Fig. 6(c). During the heating process, the diffraction peaks shift to higher angles, while the diffraction peaks present anomalous red shifts when the temperature is above 310 K, corresponding to the structural transition from RFE to SPE ones. A similar phenomenon was observed in the $Ba_4SmFe_{0.5}Nb_{9.5}O_{30}$ system [43]. The reduction of the cell parameters on the temperature range of $T_f$-$T_m$ may be related to the Debye relaxation, while the wide distribution of domains and their interactions produce a huge relaxation phenomenon with increasing the temperature. The interactions and collisions of domain structures lead to the reduction of lattice volume. As temperatures above $T_m$, the nanodomains shrink further and the interdomain coupling is weakened accordingly. The polar microregions are in a condition of dynamic disorder and the lattice thermal expansion dominates, leading to the shift of the lattice diffraction peaks to lower angles and the increase of the cell parameters. In addition, the lattice parameters vary different slopes over different temperature regions, which could be related to the structure evolution. When the temperature exceeds $T_B$, the polar domains are eliminated and the structure transforms into a PE phase. The evolution of the lattice structure is directly related to the thermal expansion, resulting in a larger slope in the PE ones.

To further investigate the structural evolution procedure and mechanism for NN-SBT-BMZ ceramics, temperature-dependent Raman spectroscopy was used to elucidate the thermally induced phonon behavior. The spectral evolution of NN-SBT-BMZ04 under temperature can be seen in Fig. 7(a), where the fitting process is displayed at the bottom. There is a high sensitivity of the Raman scattering spectra to the evolution of the lattice under temperature. The spectra exhibit a continuous variation, showing a significant decrease

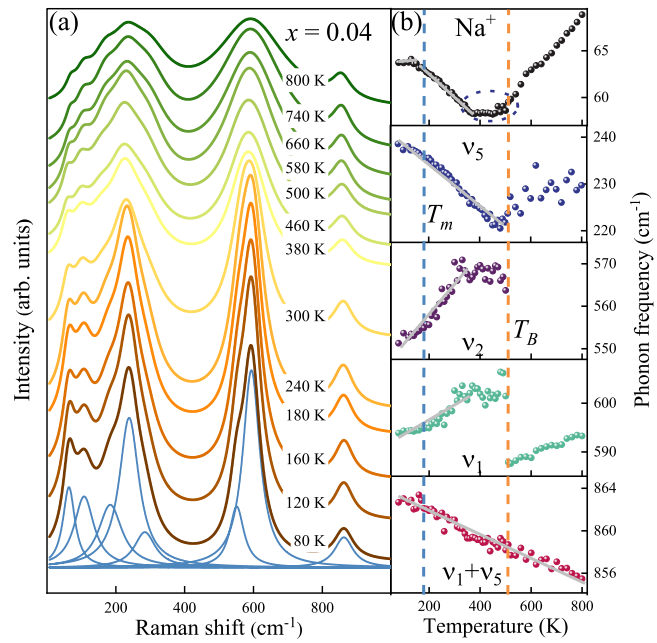


FIG. 7. (a) Temperature-dependent Raman spectra of NN-SBT-BMZ04, while the fitting process was displayed at the bottom. (b) The frequency evolutions of the main phonons of NN-SBT-BMZ04 ceramics with the temperature.

TABLE II. The center frequencies of the main phonon for RFE, SPE, and PE ones in NN-SBT-BMZ sample. The error bars were obtained by taking into account high reliability fitting process as well as the contribution of the thermal expansion.

| $x = 0.04$ | $Na^+$ | $\upsilon_1$ | $\upsilon_2$ | $\upsilon_5$ | $\upsilon_1+\upsilon_5$ | $x = 0.08$ | $Na^+$ | $\upsilon_1$ | $\upsilon_2$ | $\upsilon_5$ | $\upsilon_1+\upsilon_5$ |
|---|---|---|---|---|---|---|---|---|---|---|---|
| RFE | 63.6 | 594.4 | 553.4 | 237.3 | 862.7 | RFE | 64.1 | 594.3 | 556.5 | 235.4 | 854 |
| <170 K | ±0.5 | ±0.5 | ±2.1 | ±1.4 | ±0.7 | <190 K | ±0.6 | ±2.3 | ±4.9 | ±0.6 | ±0.7 |
| SPE | 59.8 | 600.1 | 564.9 | 228.1 | 860.1 | SPE | 60.8 | 601.2 | 566.4 | 229.34 | 852.2 |
| 170–510 K | ±3.7 | ±6.3 | ±10 | ±7.7 | ±2 | 190–460 K | ±2.1 | ±5.1 | ±7.3 | ±4.9 | ±1.2 |
| PE | 64.1 | 590.6 | - | 228.3 | 857 | PE | 62.5 | 586.9 | - | 228.4 | 850.5 |
| >510 K | ±4.8 | ±3 | - | ±4.6 | ±1.7 | >460 K | ±7.3 | ±2.7 | - | ±5.6 | ±1.6 |
| $x = 0.12$ | $Na^+$ | $\upsilon_1$ | $\upsilon_2$ | $\upsilon_5$ | $\upsilon_1+\upsilon_5$ | $x = 0.16$ | $Na^+$ | $\upsilon_1$ | $\upsilon_2$ | $\upsilon_5$ | $\upsilon_1+\upsilon_5$ |
| RFE | 61.4 | 597.3 | 560.1 | 235 | 847.2 | RFE | 58.9 | 598.2 | 557.4 | 236.3 | 842.7 |
| <230 K | ±1 | ±3.3 | ±5.4 | ±2.3 | ±0.8 | <260 K | ±1.2 | ±1.7 | ±1.9 | ±3.2 | ±1.3 |
| SPE | 58.9 | 601.3 | 562.8 | 229.7 | 845.9 | SPE | 57.5 | 601.1 | 561.2 | 233.3 | 842.1 |
| 230–440 K | ±1.4 | ±3.6 | ±6 | ±2.8 | ±1.1 | 260-360 K | ±0.6 | ±1.2 | ±3 | ±1.6 | ±0.8 |
| PE | 58.7 | 583 | - | 228.2 | 845.2 | PE | 56.9 | 579.6 | - | 230.4 | 840.6 |
| >440 K | ±2.4 | ±1.3 | - | ±4.9 | ±1.8 | >360 K | ±1.2 | ±3.6 | - | ±2.5 | ±2.3 |

in intensity with increasing the temperature. The peaks of the $\upsilon_1$ and $\upsilon_2$ phonon modes merge into a major broadening peak with increasing the temperature. Figure 7(b) shows the variation of the main phonon frequencies of NN-SBT-BMZ04 with temperature. In the range of 80–500 K, the $Na^+$ and $\upsilon_5$ and $\upsilon_1+\upsilon_5$ frequencies shift to the low wave number region with increasing the temperature, while the frequencies of $\upsilon_1$ and $\upsilon_2$ phonons shift to the high wave number. It is worth noting the frequency of the $Na^+$ vibration around the 60 $cm^{-1}$ is insensitive in the temperature range of 80–170 K. As the temperature exceeds 170 K, the $Na^+$ vibration around the 60 $cm^{-1}$ appears red shifted, which may be related to the RFE/SPE transition. When the temperature exceeds 500 K, the $Na^+$ and $\upsilon_5$ show anomalous frequency shifts, which may reflect the evolution of the NN-SBT-BM from the SPE to the PE phase. Interestingly, the frequencies of the $Na^+$, $\upsilon_1$, and $\upsilon_2$ show oscillations in the temperature range below the $T_B$. This is caused by the fact that the static displacement of the atoms in the crystal with respect to their PE phase equilibrium position does not occur simultaneously. There are clusters or microdomains of atoms already formed in the crystal when the temperature is below the $T_B$ temperature, while the atoms are already statically displaced with respect to the equilibrium position of the high-temperature phase. These clusters or microdomains already possess the characteristics of the low-temperature one, where the locations of the atoms is called the quasiequilibrium position. The atoms move thermally around their quasiequilibrium positions inside the microdomains, while the evolution reflected in the lattice dynamics is not obvious. As the temperature continues to decrease, the atomic correlation length in the crystal becomes increasingly large, thus increasing the size of the cluster or microdomain. The thermally induced phonon behavior for the rest ceramics agrees with that of NN-SBT-BMZ04 except for the critical temperature, while the $T_m$ and $T_B$ temperature gradually approach with increasing BMZ content. Thus, the structural evolution of the NN-SBT-BMZ ceramic under the thermal field can be clearly revealed by Raman spectra. In order to elucidate the particulars of the phonon evolution process and threshold point of NN-SBT-BMZ ceramics on different ones, the fitting frequencies for the main phonons have been concluded in Table II.

Last but not least, the evolution of the optical transition behavior of NN-SBT-BMZ ceramics under the thermal field was explored. The dielectric functions of NN-SBT-BMZ04 exhibit a significant downward trend with increasing the temperature, where the peak of the real part of the dielectric functions displays a red shift tendency, as shown in Fig. 8(a). Figure 8(b) shows the temperature dependence $E_g$ of NN-SBT-BMZ04. There is no significant variation in the optical band gap as the temperature increases from 300–450 K, while the optical band gap appears a significantly reducing trend when the temperature exceeds 450 K. The evolution process of band gap can be generally explained by the lattice thermal expansion effect and electron-phonon interaction [44]. The optical band-gap evolution is not sensitive in the temperature range of $T_m$-$T_B$, due to the competition between interdomain coupling and thermal expansion effect. The evolution of the optical band gap is directly related to the thermal expansion and thermally induced oxygen vacancies when the structure is transformed into the PE phase, exhibiting a significant decrease with increasing temperature. Therefore, the band gap appears to decrease significantly with increasing temperature when the temperature is above $T_B$. The thermally induced evolution of $E_g$ for others also agrees with that of NN-SBT-BMZ04, besides the transition temperature. It is worth noting

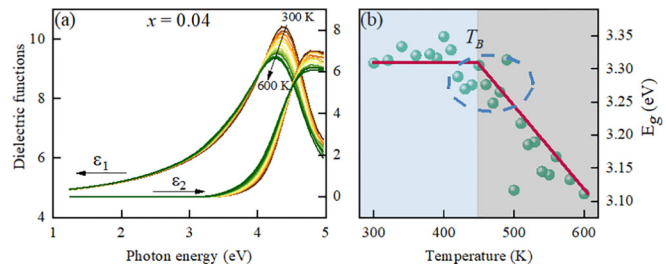


FIG. 8. (a) Temperature-dependent the dielectric functions of NN-SBT-BMZ04. (b) The band gap evolutions of the NN-SBT-BMZ04 ceramics under temperature.

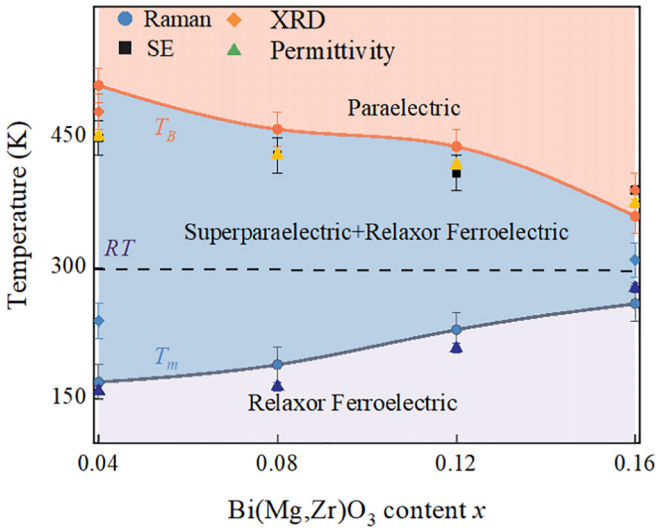


FIG. 9. The phase diagram with the Bi(Mg, Zr)$O_3$ content and temperature for the NN-SBT-BMZ samples obtained by dielectric, Raman, XRD, and SE data, respectively.

that the temperature-dependent optical transition behavior is closely matched with the results of Raman spectra, XRD, and dielectric spectra.

Overall, a detailed phase diagram of NN-SBT-BMZ ceramics with a content temperature shown in Fig. 9 was derived by combining dielectric, XRD, Raman, and SE experiments. The $T_B$ temperature exhibits a decreasing trend with the increasing BMZ content. Meanwhile, the $T_m$ temperature moves toward high temperature as the doping content is raised, which facilitates the construction of the RFE/SPE phase boundary near room temperature and enhances the energy storage properties [4,45]. However, we have identified that the energy storage density of NN-SBT-BMZ12 is the highest instead of NN-SBT-BMZ16, although NN-SBT-BMZ16 is closer to the room-temperature RFE/SPE phase boundary. This may be due to the fact that the NN-SBT-BMZ16 ceramic is also close to the SPE/PE phase boundary, causing a sharp decrease in the maximum polarization ($P_{max}$) and leading to a decrease in energy storage density. The NN-SBT-BMZ12 has the highest breakdown strength and moderate $P_{max}$ value and is located at the RFE/SPE phase boundary, thus achieving the best overall energy storage performance.

## IV. CONCLUSION AND OUTLOOK

In conclusion, this paper has investigated a detailed study of the lattice structure, phonon behavior, and optical transition for the NN-SBT-BMZ SPE energy storage ceramics. The evolution of the cell volume and optical band gap under chemical doping and temperature has been elucidated by XRD, and SE, which are closely related to the interaction of interdomain coupling and the competition of lattice thermal expansion. Notably, the oscillatory processes of the main phonons near the $T_B$ temperature clearly reflect the relaxation state of the lattice structure. Finally, the $T_m$ and $T_B$ temperatures obtained from the thermally induced dielectric, lattice parameter, phonon behaviors, and $E_g$ evolutions are relatively consistent, where the condensed matter spectroscopy is a significant tool for studying the structural properties and evolution mechanisms of RFE/SPE/PE ones. This paper will enhance the whole understanding of the lattice dynamics, optical transitions, and structural transformations for SPE $NaNbO_3$-based ceramics, and facilitate the development of energy storage materials and their applications.

## ACKNOWLEDGMENTS

This work was financially supported by the National Natural Science Foundation of China (Grants No. 62090013, No. 61974043, and No. 12104156), the National Key Research and Development Program of China (Grant No. 2019YFB2203403), the Projects of Science and Technology Commission of Shanghai Municipality (Grants No. 21JC1402100 and No. 23ZR1446400), the Natural Science Foundation of Chongqing, China (CSTB2022NSCQ-MSX1367), and the Program for Professor of Special Appointment (Eastern Scholar) at Shanghai Institutions of Higher Learning.

[1] H. Qi, A. W. Xie, and R. Z. Zuo, Local structure engineered lead-free ferroic dielectrics for superior energy-storage capacitors: A review, Energy Storage Mater. **45**, 541 (2022).

[2] L. Chen, S. Q. Deng, H. Liu, J. Wu, H. Qi, and J. Chen, Giant energy-storage density with ultrahigh efficiency in lead-free relaxors via high-entropy design, Nature Commun. **13**, 3089 (2022).

[3] J. Shi, Y. X. Zhao, J. Y. He, T. Y. Li, F. Y. Zhu, W. C. Tian, and X. Liu, Deferred polarization saturation boosting superior energy-storage efficiency and density simultaneously under moderate electric field in relaxor ferroelectrics, ACS Appl. Energy Mater. **5**, 3436 (2022).

[4] H. Pan, S. Lan, S. Qi, Q. H. Zhang, H. B. Yao, Y. Q. Liu, F. Q. Meng, E. J. Guo, L. Gu, D. Yi, X. R. Wang, and H. B. Huang, J. L. MacManus-Driscoll, L. Q. Chen, K. J. Jin, C. W. Nan, and Y. H. Lin, Ultrahigh energy storage in superparaelectric relaxor ferroelectrics, Science **374**, 100 (2021).

[5] J. Chen, Y. Zhou, X. Y. Huang, C. Y. Yu, Q. L. Han, A. Wang, Y. Zhu, K. Shi, Q. Kang, P. L. Li, P. K. Jiang, X. S. Qian, H. Bao, S. T. Li, G. N. Wu, X. Y. Zhu, and Q. Wang, Ladderphane copolymers for high-temperature capacitive energy storage, Nature (London) **615**, 62 (2023).

[6] H. Qi, W. C. Li, L. Wang, L. Chen, H. Liu, S. Q. Deng, and J. Chen, Large (anti)ferrodistortive $NaNbO_3$-based lead-free relaxors: Polar nanoregions embedded in ordered oxygen octahedral tilt matrix, Mater. Today **60**, 91 (2022).

[7] A. W. Xie, J. Fu, R. Z. Zuo, X. W. Jiang, T. Y. Li, Z. Q. Fu, Y. W. Yin, X. G. Li, and S. J. Zhang, Supercritical relaxor nanograined ferroelectrics for ultrahigh-energy-storage capacitors, Adv. Mater. **34**, 2204356 (2022).

[8] Z. Y. Che, L. Ma, G. G. Luo, C. Xu, Z. Y. Cen, Q. Feng, X. Y. Chen, K. L. Ren, and N. N. Luo, Phase structure and defect engineering in $(Bi_{0.5}Na_{0.5})TiO_3$-based relaxor antiferroelectrics

toward excellent energy storage performance, Nano Energy **100**, 107484 (2022).

[9] Z. J. Jiang, S. Prosandeev, and L. Bellaiche, Energy storage in lead-free Ba(Zr, Ti)$O_3$ relaxor ferroelectrics: Large densities and efficiencies and their origins, Phys. Rev. B **105**, 024102 (2022).

[10] W. Wang, L. Y. Zhang, R. Y. Jing, Q. Y. Hu, D. D. Alikin, V. Y. Shur, X. Y. Wei, G. Liu, Y. Yan, and L. Jin, Enhancement of energy storage performance in lead-free barium titanate-based relaxor ferroelectrics through a synergistic two-step strategy design, Chem. Eng. J. **434**, 134678 (2022).

[11] V. Westphal, W. Kleemann, and M. D. Glinchuk, Diffuse phase transitions and random-field-induced domain states of the "relaxor" ferroelectric $PbMg_{1/3}Nb_{2/3}O_3$, Phys. Rev. Lett. **68**, 847 (1992).

[12] V. V. Shvartsman and D. C. Lupascu, Lead-free relaxor ferroelectrics, J. Am. Ceram. Soc. **95**, 1 (2012).

[13] L. E. Cross, Relaxor ferroelectrics, Ferroelectrics **76**, 241 (1987).

[14] F. Li, S. J. Zhang, D. Damjanovic, L. Q. Chen, and T. R. Shrout, Local structural heterogeneity and electromechanical responses of ferroelectrics: Learning from relaxor ferroelectrics, Adv. Funct. Mater. **28**, 1801504 (2018).

[15] A. R. Jayakrishnan, J. P. B. Silva, K. Kamakshi, D. Dastan, V. Annapureddy, M. Pereira, and K. C. Sekhar, Are lead-free relaxor ferroelectric materials the most promising candidates for energy storage capacitors? Prog. Mater. Sci. **132**, 101046 (2023).

[16] G. F. Liu, L. Chen, and H. Qi, Energy storage properties of $NaNbO_3$-based leadfree superparaelectrics with large antiferrodistortion, Microstructures **3**, 2023008 (2023).

[17] H. Y. Chen, L. Liu, Z. N. Yan, X. Yuan, H. Luo, and D. Zhang, Ultrahigh energy storage density in superparaelectric-like $Hf_{0.2}Zr_{0.8}O_2$ electrostatic supercapacitors, Adv. Sci. **10**, 2300792 (2023).

[18] R. T. Li, D. M. Xu, M. Avdeev, L. Zhang, X. F. Chen, G. Y. Gou, D. Wang, W. F. Liu, and D. Zhou, Ultralow loss and high tunability in a non-perovskite relaxor ferroelectric, Adv. Funct. Mater. **33**, 2210709 (2023).

[19] K. Wang, J. Ouyang, M. M. Wuttig, Y. Y. Zhao, H. B. Cheng, Y. Zhang, R. X. Su, Y. Jing, X. L. Zhong, and F. Zeng, Superparaelectric $(Ba_{0.95}, Sr_{0.05})(Zr_{0.2}, Ti_{0.8})O_3$ ultracapacitors, Adv. Energy Mater. **10**, 2001778 (2020).

[20] S. K. Mishra, N. Choudhury, S. L. Chaplot, P. S. R. Krishna, and R. Mittal, Competing antiferroelectric and ferroelectric interactions in $NaNbO_3$: Neutron diffraction and theoretical studies, Phys. Rev. B **76**, 024110 (2007).

[21] S. K. Mishra, M. K. Gupta, R. Mittal, M. Zbiri, S. Rols, H. Schober, and S. L. Chaplot, Phonon dynamics and inelastic neutron scattering of sodium niobate, Phys. Rev. B **89**, 184303 (2014).

[22] H. D. Megaw, The seven phases of sodium niobat, Ferroelectrics **7**, 87 (1974).

[23] C. N. W. Darlington and K. S. Knight, On the lattice parameters of sodium niobate at room temperature and above, Phys. B: Condens. Matter **266**, 368 (1999).

[24] Z. Q. Xu, Z. Liu, K. Dai, T. Lu, Z. Q. Lv, Z. G. Hu, Y. Liu, and G. S. Wang, Simultaneously achieving large energy density and high efficiency in $NaNbO_3 - (Sr, Bi)TiO_3 - Bi(Mg, Zr)O_3$ relaxor ferroelectric ceramics for dielectric capacitor applications, J. Mater. Chem. A **10**, 13907 (2022).

[25] A. Y. Cui, Y. Ye, L. M. Zheng, K. Jiang, L. Q. Zhu, L. Y. Shang, Y. W. Li, Z. G. Hu, and J. H. Chu, Exploring lattice symmetry evolution with discontinuous phase transition by Raman scattering criteria: The single-crystalline (K, Na)$NbO_3$ model system, Phys. Rev. B **100**, 024102 (2019).

[26] H. F. Geng, J. W. Chen, J. Jiao, Y. P. Guo, D. Viehland, and H. S. Luo, Investigation of lattice evolutions of tetragonal $(Na_{0.5}Bi_{0.5})TiO_3 - BaTiO_3$ single crystal by phonon modes in Raman scattering, Scr. Mater. **225**, 115184 (2023).

[27] Y. Ye, A. Y. Cui, M. Y. Bian, K. Jiang, L. Q. Zhu, J. Z. Zhang, L. Y. Shang, Y. W. Li, Z. G. Hu, and J. H. Chu, Temperature and pressure manipulation of magnetic ordering and phonon dynamics with phase transition in multiferroic $GdFeO_3$: Evidence from Raman scattering, Phys. Rev. B **102**, 024103 (2020).

[28] K. Dai, A. Y. Cui, Z. Liu, K. Jiang, J. Z. Zhang, Y. W. Li, G. S. Wang, X. L. Dong, and Z. G. Hu, Pressure-driven explosive energy conversion in lead-free ferroelectric (Ag, K)$NbO_3$, Phys. Rev. Appl. **19**, 054058 (2023).

[29] K. Dai, A. Y. Cui, Y. Ye, K. Jiang, J. Z. Zhang, Y. W. Li, G. S. Wang, X. L. Dong, Z. G. Hu and J. H. Chu, Phase diagram with an antiferroelectric/ferroelectric phase boundary in $AgNbO_3 - LiTaO_3$ energy-storage ceramics by lattice dynamics and electronic transitions, Phys. Rev. B **104**, 174104 (2021).

[30] E. Buixaderas, I. Gregora, J. Hlinka, J. Dec, and T. Lukasiewicz, Raman and IR phonons in ferroelectric $Sr_{0.35}Ba_{0.69}Nb_2O_{6.04}$ single crystals, Phase Transit. **86**, 217 (2013).

[31] F. H. Pang, X. L. Chen, C. C. Sun, J. P. Shi, X. Li, H. Y. Chen, X. Y. Dong, and H. F. Zhou, Ultrahigh energy storage characteristics of sodium niobate-based ceramics by introducing a local random field, ACS Sustainable Chem. Eng. **8**, 14985 (2020).

[32] J. M. Ye, G. S. Wang, M. X. Zhou, N. T. Liu, X. F. Chen, S. Li, F. Cao, and X. L. Dong, Excellent comprehensive energy storage properties of novel lead-free $NaNbO_3$-based ceramics for dielectric capacitor applications, J. Mater. Chem. C **7**, 5639 (2019).

[33] N. Qu, H. L. Du, and X. H. Hao, A new strategy to realize high comprehensive energy storage properties in lead-free bulk ceramics, J. Mater. Chem. C **7**, 7993 (2019).

[34] M. Z. Xie, M. Li, L. M. Li, J. Z. Zhang, K. Jiang, L. Y. Shang, Y. W. Li, Z. G. Hu, and J. H. Chu, Temperature-dependent phonon mode and interband electronic transition evolutions of $\epsilon -$ InSe films derived by pulsed laser deposition, Appl. Phys. Lett. **117**, 102101 (2020).

[35] T. T. Qi, M. T. Curnan, S. Kim, J. W. Bennett, I. Gtinberg, and A. M. Rappe, First-principles study of band gap engineering via oxygen vacancy doping in perovskite $ABB'O_3$ solid solutions, Phys. Rev. B **84**, 245206 (2011).

[36] L. Zhang, H. Hao, S. J. Zhang, M. T. Lanagan, Z. H. Yao, Q. Xu, J. Xie, J. Zhou, M. H. Cao, and H. X. Liu, Defect structure-electrical property relationship in Mn-doped calcium strontium titanate dielectric ceramics, J. Am. Ceram. Soc. **100**, 4638 (2017).

[37] F. Li, J. W. Zhai, B. Shen, X. Liu, and H. R. Zeng, Simultaneously high-energy storage density and responsivity in quasi-hysteresis-free Mn-doped $Bi_{0.5}Na_{0.5}TiO_3 - BaTiO_3 -$

$(Sr_{0.7}Bi_{0.2})TiO_3$ ergodic relaxor ceramics, Mater. Res. Lett. **6**, 345 (2018).

[38] A. A. Bokov and Z. G. Ye, Dielectric relaxation in relaxor ferroelectrics, J. Adv. Dielect. **02**, 1241010 (2012).

[39] G. Burns and F. H. Dacol, Glassy polarization behaviour in ferroelectric compounds $Pb(Mg_{1/3}Nb_{2/3})O_3$ and $Pb(Zn_{1/3}Nb_{2/3})O_3$, Solid State Commun. **48**, 853 (1983).

[40] W. C. Liu, W. Zhou, R. Sooryakumar, and C. L. Mak, Inelastic light scattering studies of diffuse phase transition in ferroelectric $Sr_{1.9}Ca_{0.1}NaNb_5O_{15}$ thin films, J. Raman Spectrosc. **43**, 326 (2012).

[41] A. J. Bell, Calculations of dielectric properties from the superparaelectric model of relaxors, J. Phys.: Condens. Matter **5**, 8773 (1993).

[42] Y. Li, W. Lin, B. Yang, S. M. Zhang, and S. F. Zhao, Domain dynamics engineering in ergodic relaxor ferroelectrics for dielectric energy storage, Acta Mater. **255**, 119071 (2023).

[43] C. Z. Hu, S. Zhen, Z. Sun, Q. H. Zhu, F. Q. Lu, C. C. Li, L. J. Liu, and L. Fang, Relaxor behavior and ferroelectric properties of a new $Ba_4SmFe_{0.5}Nb_{9.5}O_{30}$ tungsten bronzeceramic, Ceram. Int. **42**, 14999 (2016).

[44] Z. H. Duan, Z. G. Hu, K. Jiang, Y. W. Li, X. L. Dong, and J. H. Chu, Temperature-dependent dielectric functions and interband critical points of relaxor lead hafnate-modified $PbSc_{1/2}Ta_{1/2}O_3$ ferroelectric ceramics by spectroscopic ellipsometry, Appl. Phys. Lett. **102**, 151908 (2013).

[45] W. J. Cao, P. F. Chen, R. J. Lin, F. Li, B. H. Ge, D. S. Song, Z. X. Cheng, and C. C. Wang, Boosting energy-storage performance in lead-free ceramics via polyphase engineering in the superparaelectric state, Compos. B. Eng. **255**, 110630 (2023).